processes

MDPI

Article

Bifunctional Electrocatalysts for Alkaline Water Electrolysis Derived from Metal-Containing Ionic Liquids

Jelena Georgijević [1], Nikola Zdolšek [1], Milica Vasić [2], Jadranka Milikić [2], Milan Vraneš [3], Dragana Jugović [4], Diogo M. F. Santos [5] and Biljana Šljukić [2,5,*]

[1] Department of Physical Chemistry, "Vinča" Institute of Nuclear Sciences—National Institute of the Republic of Serbia, University of Belgrade, Mike Petrovića Alasa 12–14, 11351 Belgrade, Serbia; georgijevic@vin.bg.ac.rs (J.G.); zdolsek@vin.bg.ac.rs (N.Z.)
[2] University of Belgrade, Faculty of Physical Chemistry, Studentski trg 12–16, 11158 Belgrade, Serbia; mvasic@ffh.bg.ac.rs (M.V.); jadranka@ffh.bg.ac.rs (J.M.)
[3] Department of Chemistry, Biochemistry and Environmental Protection, Faculty of Sciences, University of Novi Sad, Trg Dositeja Obradovića 3, 21000 Novi Sad, Serbia; milan.vranes@dh.uns.ac.rs
[4] Institute of Technical Sciences of SASA, Knez Mihailova 35/IV, 11000 Belgrade, Serbia; dragana.jugovic@itn.sanu.ac.rs
[5] Center of Physics and Engineering of Advanced Materials, Laboratory for Physics of Materials and Emerging Technologies, Chemical Engineering Department, Instituto Superior Tecnico, Universidade de Lisboa, 1049-001 Lisbon, Portugal; diogosantos@tecnico.ulisboa.pt
* Correspondence: biljana.paunkovic@tecnico.ulisboa.pt

Abstract: Carbon-based electrocatalysts decorated with Pt and Ni nanoparticles were introduced herein to increase the efficiency of the water splitting process and thus reduce the price of the produced green hydrogen. The materials were prepared by innovative direct carbonization of ionic liquids containing the corresponding metal, thereby eliminating the need for additional solutions and templates. The structural integrity of the materials was validated through X-ray diffraction analysis and Fourier-transform infrared spectroscopy. The electrochemical performance of these materials in catalyzing hydrogen (HER) and oxygen (OER) evolution reactions was evaluated using voltammetry and electrochemical impedance spectroscopy, uncovering distinct behaviors and highlighting the role of ionic liquid in tailoring materials' properties and performance. Specifically, the presence of Ni was observed to enhance the catalytic performance towards the HERs due to the interaction of Ni nanoparticles and a higher amount of sp^2-hybridized carbon present. In contrast, incorporating Pt into the carbon matrix was found to augment the catalytic activity for OERs with a Tafel slope of 129 mV dec^{-1} and a current density of 10 mA cm^{-2} reached at a potential of 1.67 V. Moreover, chronoamperometric measurements evidenced materials' steady performance under both HER and OER conditions. These findings of good activity and stability showed that the introduced approach of synthesis of carbon electrocatalysts decorated with heteroatoms by direct carbonization of ionic liquids holds great promise for the synthesis of efficient and affordable electrocatalysts for green hydrogen production.

Keywords: platinum; nickel; carbon; metal-containing ionic liquids; hydrogen evolution reaction; oxygen evolution reaction

check for updates

Academic Editors: Christos Argirusis, Mingpeng Chen, Huachuan Sun and Yuxiao Zhang

Received: 4 December 2024
Revised: 28 January 2025
Accepted: 19 February 2025
Published: 22 February 2025

Citation: Georgijević, J.; Zdolšek, N.; Vasić, M.; Milikić, J.; Vraneš, M.; Jugović, D.; Santos, D.M.F.; Šljukić, B. Bifunctional Electrocatalysts for Alkaline Water Electrolysis Derived from Metal-Containing Ionic Liquids. *Processes* **2025**, *13*, 623. https://doi.org/10.3390/pr13030623

Copyright: © 2025 by the authors. Licensee MDPI, Basel, Switzerland. This article is an open access article distributed under the terms and conditions of the Creative Commons Attribution (CC BY) license (https://creativecommons.org/licenses/by/4.0/).

1. Introduction

Fossil fuels, such as coal, oil, and natural gas, are economically affordable due to their simple extraction, processing, and distribution to consumers [1]. Consequently, they currently account for 85% of global primary energy production. However, their use is jeopardized by greenhouse gas emissions during their combustion and limited reserves.

These issues related to the exploitation of fossil fuels will inevitably lead to an increase in their costs.

Hydrogen (H_2) is an emission-free fuel that does not produce greenhouse gases or other harmful emissions (such as CO_2), making it one of the most promising fuels of the future. There are numerous ways to produce hydrogen: it can be obtained from fossil fuels (coal, natural gas), through nuclear energy, as well as from renewable energy sources [2]. The purest hydrogen is produced through water electrolysis, but this process is very expensive at the moment [3]. For this reason, only 4–5% of global H_2 is currently produced via water electrolysis [4]. The efficiency of this process depends on various factors, such as electrode materials, temperature and pressure, and electrolyte composition [5]. The high cost of water-electrolysis hydrogen makes it economically unfeasible for widespread application.

Platinum (Pt)-based electrocatalysts demonstrate superior performance for hydrogen evolution reaction (HER); however, their high cost makes them unsuitable for broader applications. As a result, nickel (Ni)-based materials are used as electrodes in alkaline solutions [6]. These materials offer good chemical stability, corrosion resistance, and are more affordable than Pt-based electrocatalysts. In recent times, non-platinum catalysts based on carbides, sulfides, and phosphides have been investigated for HER [7,8]. Research on the influence of cathode material on the process of water electrolysis included, for instance, nickel-cadmium (Ni-Cd), iron-phosphorus (Fe-P), iron-phosphorus-cerium (Fe-P-Ce), and cobalt-iron phosphide nanosheets over nickel foam (CoFe-P/NF) [9–13].

Materials for oxygen evolution reaction (OER) that exhibit good activity and stability across all pH values are primarily noble metal-based materials (e.g., iridium (Ir) and ruthenium (Rh) oxides). However, their practical application is again limited due to their high cost and scarce availability. Consequently, research efforts have been directed toward developing alternative materials for OER. Various alloys and oxides, as well as carbon-based materials (such as graphene, graphene oxide, and carbon nanotubes), have been developed for OER catalysis [14–17]. Transition metal oxides have attracted significant interest in water electrocatalysis reactions (OER/HER). Due to their affordable cost, excellent corrosion resistance, and multivalent oxidation states ($M^{2+/3+/4+}$), cobalt and nickel oxides are suitable candidates for electrode materials in OER [14,18–20]. NiO has garnered significant attention in various fields, such as electrolysis. Considerable efforts have been devoted to enhancing the activity of NiO by tuning its particle size, surface, and microstructural morphology [9]. Furthermore, higher oxidation states of Ni, such as Ni^{3+}, are highly active for OER, so many studies have been conducted to produce higher oxidation states of Ni along with good crystalline structures of NiO [21]. Mixed Ni-Fe electrocatalysts have also been extensively studied as OER catalysts in alkaline solution [22].

Transition metals and their compounds are often integrated with carbon nanomaterials for more efficient electrochemical water splitting due to an increase in conductivity, specific surface area, and stability upon integration with carbon materials [23]. The simplification of the synthesis procedure, as well as the possibility of controlling the morphology, architecture, and interface engineering of the metal-carbon materials could contribute to the development of efficient and affordable electrocatalysts for water splitting.

Ionic liquids (ILs) have been suggested for catalysis of electrochemical water-splitting reactions as (i) heteroatom (e.g., N, S, P, B) dopants during electrocatalysts' synthesis preparation [24,25], (ii) metal sources during electrocatalysts' synthesis [24,26], and (iii) electrocatalysts themselves [27–30].

Carbon materials decorated with metal nanoparticles are typically prepared by carbonization of C-rich precursors, for instance, by hydrothermal carbonization of raw biomass at high temperatures in the presence of a suitable metal nanoparticle precursor. Preparation of carbon materials decorated with metal nanoparticles by direct carbonization of ILs

brings advantages in terms of both markedly simplified synthesis procedure and tunability of carbon materials' properties such as morphology, specific surface area, and surface functionalities. Specifically, the suggested one-step synthesis procedure is rather simple, with ILs acting simultaneously as a single carbon and metal nanoparticles precursor and medium (eliminating the need to use other solvents). ILs are C-rich, and, at the same time, numerous combinations of anion–cation pairs provide the possibility of designing a vast number of different ILs and, consequently, carbon materials with heteroatom dopants or metal nanoparticles. ILs act as structure-directing agents and templates for porosity creation without the need for additional templates (unlike the need to use silica templates in hydrothermal carbonization), producing carbon materials with task-desired properties, including high porosity and high specific surface area [31]. Such tailored metal-containing carbon materials can be used as efficient and economically viable electrocatalysts for producing green hydrogen by electrochemical water splitting [26,31,32] and other green energy-related applications [33].

The present work aims to contribute to the advancement in green hydrogen production by identifying an optimal bifunctional metal nanoparticles/carbon catalyst for electrochemical water splitting. Thus, Ni/C and Pt/C catalysts will be prepared by one-step, direct carbonization of ionic liquids containing metal and, for the first time, studied systematically for HER and OER, correlating their structural and morphological properties with their electrochemical performance. Among a wide range of ionic liquids, 1-alkyl-3-methylimidazolium chloride has been selected because ionic liquids with chloride anions readily form complexes with metal chlorides. By combining chloride-based ionic liquids with metal-chloride salts, transition metal chloride complexes (e.g., tetrachloronickelate, tetrachloroplatinate) can be easily synthesized. This approach renders the preparation of metal-containing ionic liquids both efficient and straightforward. Second, imidazolium ionic liquids were selected for their remarkable stability, particularly due to the robustness of the imidazolium ring structure [34]. This stability makes them highly suitable for carbonization processes, enabling the synthesis of carbon-based materials. The deep understanding of tailoring materials' properties via the choice of ionic liquid precursors to reach superior performance towards water splitting opens the possibility of developing exceptional electrocatalysts for hydrogen-energy-related applications.

2. Materials and Methods

2.1. Materials Synthesis and Characterization

Ionic liquids used in this study were prepared by mixing corresponding quantities of ionic liquids with chloride (Cl^-) anion: 1-hexyl-3-methylimidazolium chloride and 1-hexadecyl-3-methylimidazolium chloride, with metal (Pt or Ni, respectively) chloride salt. Then, the mixture was melted at 85 °C. Prepared 1- hexadecyl-3-methylimidazolium nickel chloride $[C_{16}mim]_2[NiCl_4]$ (prepared at the Institute of Chemical Process Fundamentals of the CAS, v.v.i. in collaboration with Magdalena Bendová and Theeranon Tankam; full details of the synthesis of this structure will be published elsewhere; ref. personal communication, January 10, 2025) and 1-hexyl-3-methylimidazolium platinum chloride $[Hmim]_2[PtCl_4]$ ionic liquids were used as received. Electrocatalysts were prepared by carbonization of two ionic liquids by heating up to 400 °C for 1 h and then up to 800 °C for another hour at a heating rate of 10 °C min^{-1}. Carbonization was performed under a nitrogen (N_2) atmosphere with an N_2 flow rate of 35 mL min^{-1}. Obtained materials were denoted as Ni/C and Pt/C, respectively.

X-ray diffraction (XRD) analysis was carried out using a Philips PW 1050 diffractometer (Phillips, Amsterdam, The Netherlands) with Cu-K$\alpha_{1,2}$ radiation (Ni filter) within 2θ range of 10–90° with a scanning step of 0.05° and 3 s per step. Fourier-transform infrared

spectroscopy (FTIR) spectra were collected on a Thermo Nicolet Avatar 370 FTIR Spectrometer (Thermo Fisher, Waltham, MA, USA). The corresponding powdered sample was mixed with a KBr solution, and a pellet was made. The spectra were recorded in the 4000–400 cm^{-1} range with 64 scans per spectrum at a resolution of 2 cm^{-1}. Thermogravimetric/differential thermal analysis (TGA/DTA) measurements were done under air flow at a heating rate of 10 K min^{-1} using the device TA SDT Model 2960 (TA Instruments, New Castle, DE, USA).

2.2. Electrochemical Measurements

Electrochemical studies were carried out using an Ivium V01107 (Eindhoven, The Netherlands) potentiostat and graphite rod as the counter electrode, a saturated calomel electrode as the reference electrode, and an 8 M KOH as the electrolyte. All potentials are presented versus reversible hydrogen electrode (RHE). As for the working electrode, catalytic ink (10 μL) was drop-casted onto a glassy carbon tip and dried at 100 °C overnight. The catalytic ink comprised a powder sample (Pt/C or Ni/C, 5 mg) and 2 wt.% polyvinylidene fluoride solution in n-methyl-2-pyrrolidone (125 μL).

The HER study was carried out by recording voltammograms from the open circuit potential (OCP) to more negative values at 2 mV s^{-1} at 25 °C. Electrochemical impedance spectroscopy (EIS) and chronoamperometry (CA) measurements were done at −0.28 V. The OER study was carried out by recording voltammograms from the OCP to more positive values at 5 mV s^{-1} at 25 °C. EIS and CA were carried out at 1.7 V.

3. Results and Discussion

3.1. Physicochemical Characterization

A material's electrocatalytic activity strongly depends on its composition, structure, morphology and textural properties, as well as surface chemistry. The composition of the prepared materials was confirmed by XRD (as qualitative analysis) and TGA/DTA (as quantitative analysis). Their structure was evaluated by XRD analysis and FTIR spectroscopy. Raman spectroscopy further gave insight into the presence of defects within the prepared materials, with these defects often giving rise to higher electrocatalytic activity. Insight into morphology was gained by scanning electron spectroscopy (SEM, Figure S1 illustrates the case of Ni/C). A higher specific surface area implies a higher number of active sites and a higher contact area of the electrocatalysts with the electrolyte with a more porous structure, favoring diffusion of charge carriers to/from the active centers.

The XRD analysis confirmed the presence of metal Pt in the Pt/C sample. All diffraction peaks can be ascribed to the $Fm\bar{3}m$ space group (No. 225) by comparison with diffraction card PDF2 No. 87-646. Figure 1A shows the diffraction pattern of Pt/C with peaks indexed according to the $Fm\bar{3}m$ space group. The diffraction pattern of the Ni/C sample confirmed the presence of metal Ni (PDF2 No. 87-712). A zoom in the diffractogram also reveals the presence of the almost undetectable amount of NiO phase (PDF2 No. 71-1179). Figure 1A also shows the diffraction pattern of sample Ni/C with peaks that belong to metal Ni indexed according to the $Fm\bar{3}m$ space group. The presence of Ni in higher oxidation states usually favors the materials' activity towards the OER; the only negligible amount of NiO present therein partially explains the absence of Ni/C activity towards OER. There was no evidence of the formation of crystalline carbon, and the internal carbon in both samples can be assumed to contribute to the background. Lattice parameters were determined by using Le Bail's whole profile unit cell refinement [35] within the FullProf program, and the obtained values are 3.9229(5) and 3.52473(2) Å for Pt and Ni, respectively. The coherent domain sizes, i.e., crystallite sizes, were calculated using the X-ray Line Profile Fitting Program (XFIT) with a Fundamental Parameters convolution approach to generating line profiles [36]. This approach considers both instrumental line broadening

and microstrain parameters. The obtained crystallite sizes were 7 and 53 nm for Pt and Ni, respectively. Metal particles' morphology (shape and size) reflects their electrocatalytic performance [31,32]. Namely, particles' size and shape are reflected in the size of facets and edges, as well as in the coordinated/undercoordinated surface atoms ratio. Consequently, controlling the nanoparticles' size and shape and preventing their agglomeration (by choice of metal-containing ionic liquid) can maximize the nanoparticles' surface reactivity [31,32]. Smaller nanoparticle size contributes to the disassociation of hydrogen molecules at the surface of a particle [37]; consequently, higher particle size in the case of Ni/C can contribute to its observed higher activity towards HER.

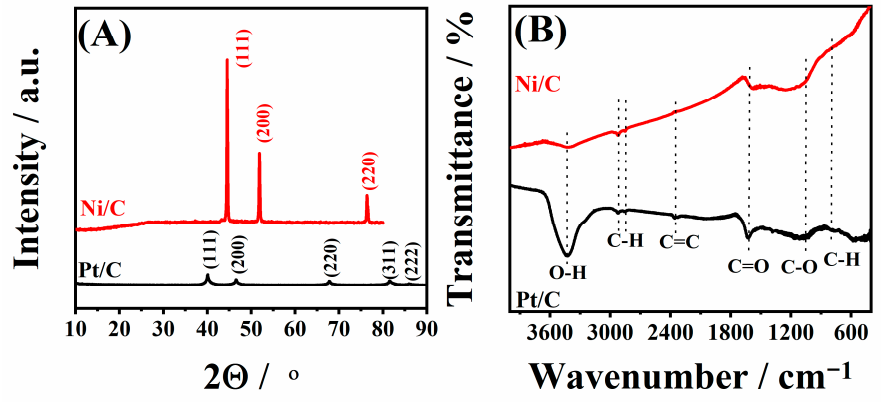


Figure 1. (**A**) XRD patterns and (**B**) FTIR spectra of Pt/C and Ni/C. The XRD peaks are indexed according to $Fm\bar{3}m$ space group.

FTIR spectra of Pt/C and Ni/C (Figure 1B) present characteristic spectra of carbon materials [38–45]. The broad peak obtained at 3432 cm^{-1} corresponds to the stretching vibration of the OH group, which originates from water absorption or OH groups present in the carbon material [38–45]. The peak at 2925 cm^{-1} was assigned to the aromatic C-H stretching vibrations originating from CH, CH_2, and/or CH_3 groups [42,44], while the peak at 2856 cm^{-1} corresponds to CH_2 symmetric stretching vibrations [40]. The weak bands at 2363, 1625, 1049, and 789 cm^{-1} were related to the presence of C=C, C=O, C-O, and out-of-plane bending vibration of C-H groups [40,41,43]. All observed peaks confirmed the successful carbonization of ionic liquids to create Pt/C and Ni/C. Moreover, the appearance of peaks corresponding to the characteristic bonds within the carbon matrix and no peaks corresponding to the carbon-metal bonds in the FTIR spectra suggested a physical interaction of metal nanoparticles with the carbon matrix.

Raman spectroscopy analysis of Pt/C and Ni/C, prepared following the same procedure, showed D- and G-bands, along with three supplementary bands related to the D band (D2, D3, D4). The band parameters (position, intensity, width) are correlated with materials' structural properties (crystallinity, disorder degree) [46]. The D-band exemplifies the degree of disorder within the material, while the G-band exemplifies the level of structural order; consequently, the I_D/I_G ratio is higher when there is a higher structural disorder within carbon material. Thus, Raman spectroscopy analysis revealed the formation of carbon structure with a high number of defects as evidenced by I_D/I_G ratios of 2.07 and 2.5 for Pt/C and Ni/C, respectively [26]. Raman analysis further revealed high crystallinity in Pt/C compared to Ni/C (I_{D3}/I_G ratio of 0.2 and 0.8 for Pt/C and Ni/C, respectively).

The TGA/DTA curves of the two materials (Figure S2) show a gradual loss of physically adsorbed water up to 100 °C. Combustion of the carbonaceous fraction is evident at temperatures of 418 and 465 °C for Pt/C and Ni/C, respectively. Ni and Pt content in the corresponding electrocatalysts was then calculated based on mass loss and found to be 17.5 and 28.8 wt.%, respectively.

3.2. Electrochemical Characterization

The electrochemical charge storage characteristics of Pt/C and Ni/C in a highly alkaline environment were investigated using cyclic voltammetry (CV). The CV profiles of Pt/C were somewhat inclined, suggesting possible ohmic resistance, while profiles of Ni/C displayed a nearly rectangular shape, indicating the accumulation of charge within the electric double layer. Additionally, the cyclic voltammograms of Pt/C and Ni/C, depicted in Figure 2C,D, maintained their fundamental shapes across different scan rates, suggesting rapid adsorption/desorption processes of electrolyte ions at the electrocatalysts' surface and stable capacitive behavior. The specific capacity of Pt/C and Ni/C, derived from cyclic voltammograms at different scan rates, declined with increasing scan rates (refer to Table 1). Notably, the specific capacity values of Ni/C exceeded those of Pt/C, implying a larger interface area in contact with the electrolyte in the case of Ni/C and consequently enhanced activity for the electrolytic generation of hydrogen. For instance, the capacitance ratio between Ni/C and Pt/C reached 23 at 20 mV s^{-1}, highlighting a significant disparity in their specific surface areas. Such difference likely originate from the difference in the amount of carbon within the parent metal-containing ionic liquids (6 C atoms in $[Hmim]_2[PtCl_4]$ vs. 39 C atoms in $[C_{16}mim]_2[NiCl_4]$) and, consequently, in the prepared metal/carbon materials.

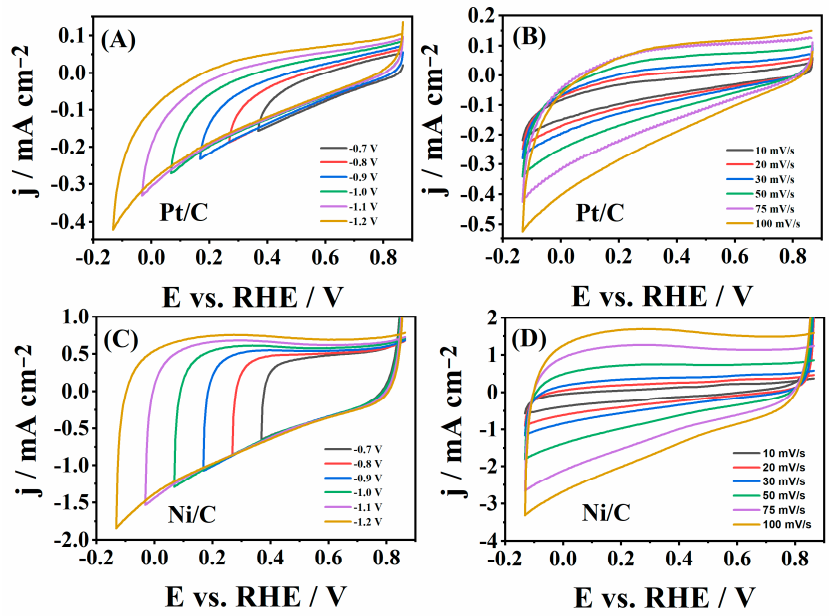


Figure 2. Cyclic voltammograms of Pt/C (**A**,**B**) and Ni/C (**C**,**D**) in deaerated 8 M KOH recorded at 50 mV s^{-1} over different cut-off potentials (**A**,**C**) and various polarization rates (**B**,**D**).

Table 1. Specific capacitance of Pt/C and Ni/C in 8 M KOH at different scan rates.

Electrocatalyst	Scan Rate/mV s^{-1}					
	10	**20**	**30**	**50**	**75**	**100**
	Capacitance/mF g^{-1}					
Pt/C	0.20	0.14	0.13	0.14	0.15	0.15
Ni/C	5.91	3.32	2.60	2.08	1.83	1.69
	Capacitance ratio					
Ni/C:Pt/C	30	24	20	15	12	11

Upon extending the cut-off potential towards more negative values below the thermodynamic threshold for the HER, i.e., below 0 V, the reduction current indicative of HER was observed in the case of Ni/C, accompanied by a corresponding peak for the oxidation of stored hydrogen on the reverse scan.

3.3. Hydrogen Evolution Reaction (HER) Study

The investigation of Pt/C and Ni/C activity for the HER in 8 M KOH revealed notably higher current densities in the case of Ni/C, Figure 3A. The reaction was found to start earlier in the case of Ni/C, with a current density of 10 mA cm^{-2} reached at a potential of −0.35 V. Conversely, Pt/C did not reach 10 mA cm^{-2} in the studied potential region. Tafel analysis was next performed by constructing the plots representing the (over)potential as a function of the logarithm of current density based on the recorded polarization curves. Tafel slope (mV dec^{-1}) represents the overpotential (mV) input necessary to raise the current by a factor of 10; the lower the Tafel slope value, the lower the overpotential necessary to attain a higher current, indicating higher electrocatalytic activity of a material. Tafel slope values of −224 mV dec^{-1} for Ni/C and −330 mV dec^{-1} for Pt/C were determined with these values significantly deviate from the theoretical values for HER (−30, −40, and −120 mV dec^{-1} for Tafel, Heyrovský, and Volmer, being the rate-determining step, respectively). Namely, HER represented by overall Equation (1) in alkaline media encompasses several steps: it starts with electrochemical hydrogen adsorption (so-called Volmer step, Equation (2)) followed by electrochemical (Heyrovsky step, Equation (3) and/or chemical (Tafel step, Equation (4)) desorption of hydrogen:

$$2H^+ + 2e^- \rightarrow H_2 \quad \text{(overall reaction)} \tag{1}$$

$$M + H_2O + e^- \rightarrow MH_{ads} + OH^- \quad \text{Volmer step} \tag{2}$$

$$MH_{ads} + H_2O + e^- \rightarrow M + H_2 + OH^- \quad \text{Heyrovský step} \tag{3}$$

$$MH_{ads} + MH_{ads} \rightarrow 2M + H_2 \quad \text{Tafel step} \tag{4}$$

Thereafter, HER can proceed by Volmer-Heyrovsky and/or Volmer-Tafel mechanism with the Tafel slope value determined by the rate-determining step.

To gain further insight into the kinetics and mechanism of HER on the studied metal-containing carbon electrodes, the EIS spectra were recorded for both metal/carbon materials at −0.28 V. The Bode plot of Pt/C, presented in Figure 3C, shows two phase angle peaks, one at intermediate to low frequencies and another at high frequencies, corresponding to two arcs in the Nyquist plot (Figure 3B) and two different time constants. In contrast, in the case of Ni/C, only one phase angle maximum can be observed at intermediate to low frequencies. The higher and lower frequency peaks of the Pt/C can be ascribed to the impedance contributions from the adsorption of the hydrogen atoms and double-layer capacitive behavior at the electrode/electrolyte interface [47], respectively. Ni/C's single arc and phase angle peak correspond to the capacitive double-layer behavior and charge-transfer kinetics.

Accordingly, the equivalent circuits in Figure 3B, inset, were used for the EIS spectra fitting and interpretation. In the presented circuits, R_s is the electrolyte resistance, R_{ct} is the charge-transfer resistance, and R_{ads} is the resistance related to hydrogen adsorption. CPE_{dl} and CPE_{ads} are constant-phase elements reflecting the double-layer capacitance and the capacitance contribution due to the adsorption of hydrogen atoms, respectively. The CPE element is used instead of ideal capacitance as an empirical element accounting for the non-ideal behavior of capacitive elements resulting from surface inhomogeneities [48]. CPE includes the parameters Q and n, where $0 < n < 1$; $n = 1$ for an ideal capacitor, and

$Z_{cpe} = Q^{-1}(i\omega)^{-n}$, (i is $\sqrt{-1}$, ω is angular frequency). The effective capacitance can be obtained from the expression $C = Q^{1/n}R^{(1-n)/n}$ [49,50].

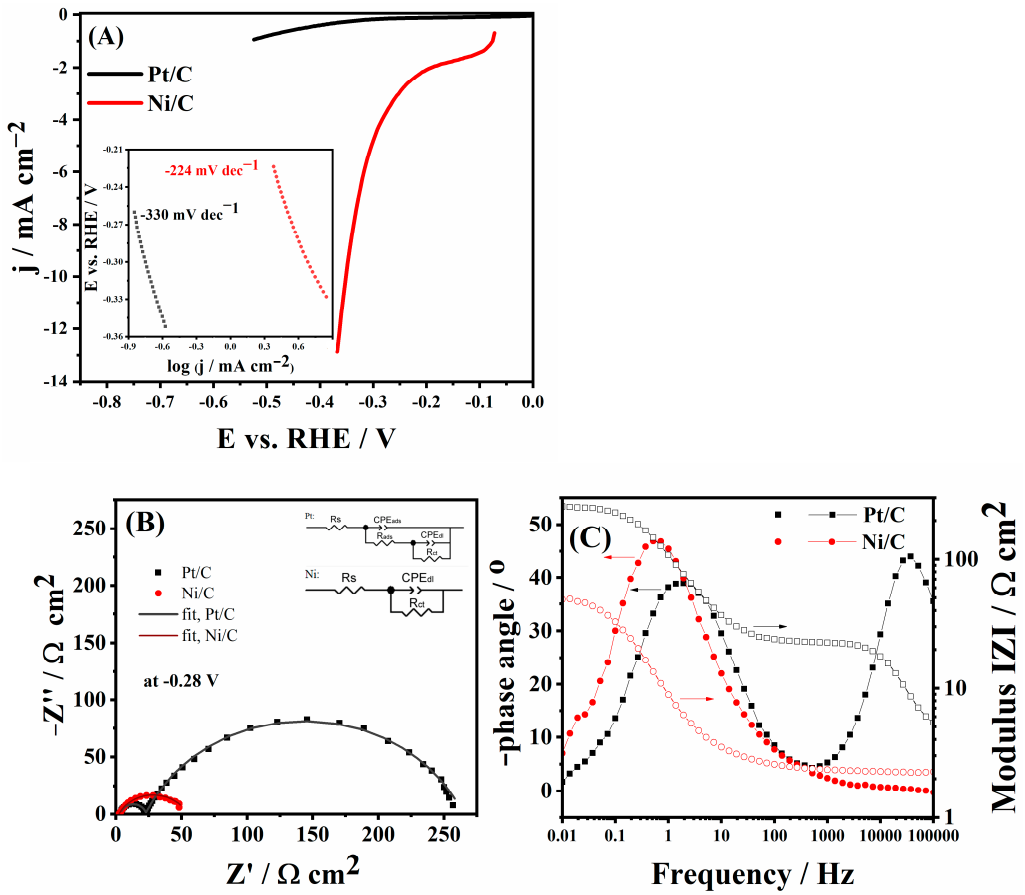


Figure 3. (**A**) Polarization curves of Pt/C and Ni/C electrocatalysts at 2 mV s^{-1}, with Tafel plots in the inset. (**B**) Nyquist and (**C**) Bode plots corresponding to the HER on Pt/C and Ni/C at −0.28 V (the arrows indicate the corresponding Y-axis). All measurements were conducted in 8 M KOH at 25 °C.

The parameters estimated by EIS spectra fitting are given in Table 2. The R_s values obtained for both samples are comparable, as expected, considering the electrolyte used in the study and the electrochemical cell setup. Regarding double-layer parameters, n values are similar for both metal/carbon materials. However, the C_{dl} values deduced from the CPE parameters suggest around 20 times larger capacitance of the Ni/C than that of the Pt/C, which is in agreement with the information derived from cyclic voltammograms, namely the specific capacity ratios, Figure 2, Table 1. Higher C_{dl} values observed for the Ni/C indicate a higher number of active sites in this electrocatalyst. This can be related to a larger fraction of carbon material in the Ni/C, which is expected based on the composition of the parent metal-containing ionic liquids (6 C atoms in $[Hmim]_2[PtCl_4]$ vs. 39 C atoms in $[C_{16}mim]_2[NiCl_4]$), as mentioned in the cyclic voltammetry part.

Table 2. EIS parameters of HER on Pt/C and Ni/C electrocatalysts, at −0.28 V, obtained by EIS spectra fitting.

	R_s (Ω cm^2)	R_{ct} (Ω cm^2)	Q_{dl} (S cm^{-2} s^n)	n_{dl}	C_{dl} (F cm^{-2})	R_{ads} (Ω cm^2)	Q_{ads} (S cm^{-2} s^n)	n_{ads}
Pt/C	3.50 ± 0.07	242 ± 2	(2.13 ± 0.03)·10^{-3}	0.75 ± 0.01	(1.69 ± 0.03)·10^{-3}	19.2 ± 0.2	(1.2 ± 0.1)·10^{-6}	0.94 ± 0.01
Ni/C	2.35 ± 0.02	52 ± 1	0.0300 ± 0.0005	0.73 ± 0.01	0.035 ± 0.001	-	-	-

Comparison of R_{ct} values reveals lower values and faster charge transfer under HER conditions in the case of Ni/C electrocatalyst, Table 2. To understand this, it should be taken into account that the electrical conductivity of carbon material is determined mostly by the amount and distribution of sp^2 sites in the material [51]. As mentioned, the I_D/I_G ratio of the Ni/C is around 20% higher than that of the Pt/C, reflecting a larger fraction of sp^2-bonded carbon in the Ni/C, i.e., a larger sp^2/sp^3 ratio [52,53]. This further results in higher electrical conductivity, better electric contact between electroactive particles, and easier charge transfer through the electrode/electrolyte interface in the case of Ni/C electrocatalyst.

Regarding the HER-related resistance, representing the sum of R_{ct} and R_{ads}, the results indicate a faster reaction rate in the case of the Ni/C electrocatalyst. This and its higher C_{dl} values undoubtedly demonstrate better HER electrocatalytic performance of the Ni/C. These findings are consistent with those obtained from polarization curves (Figure 3A).

3.4. Oxygen Evolution Reaction (OER) Study

The activity of Pt/C and Ni/C for OER in 8 M KOH was also investigated, Figure 4A. The difference in activity between the two electrocatalysts for OER is clearly seen. Specifically, Pt/C provides a higher current density than Ni/C under the same conditions. The current density of Pt/C reaches a value of 10 mA cm^{-2} at a potential of 1.67 V, while the current density of Ni/C did not attain the value of 10 mA cm^{-2} within the examined potential range. The Tafel slope is evaluated to be 129 mV dec^{-1} for Pt/C, and a higher value of 131 mV dec^{-1} is evaluated for Ni/C. OER represented by overall Equation (5) in alkaline media encompasses several steps (Equations (6)–(10)). The OER mechanism is intricate and requires the sequential transfer of four electrons, starting with the interaction of OH^- ions on the electrocatalyst surface. Initially, OH^- adsorbs and undergoes a 1 e^- oxidation to form MOH (Equation (6)), which subsequently converts into MO through the loss of one proton and one electron (Equation (7)). Two MO species can recombine to generate O_2, thereby freeing two active sites (Equation (8)). Alternatively, MO can react with an OH^- ion through 1 e^- oxidation, forming MOOH (Equation (9)), which undergoes proton-coupled electron transfer to produce O_2 while liberating one active site (Equation (10)).

$$4OH^- \rightarrow 2O_2 + 2H_2O + 4e^- \quad \text{(overall reaction)} \tag{5}$$

$$M + OH^- \rightarrow MOH + e^- \tag{6}$$

$$MOH + OH^- \rightarrow MO + H_2O_{(l)} + e^- \tag{7}$$

$$2MO \rightarrow 2M + O_{2(g)} \tag{8}$$

$$MO + OH^- \rightarrow MOOH + e^- \tag{9}$$

$$MOOH + OH^- \rightarrow M + O_{2(g)} + H_2O_{(l)} + e^- \tag{10}$$

Table 3 compares the performance of different electrocatalysts based on Pt and Ni for OER in an alkaline medium. The Pt/C prepared therein shows a Tafel slope value lower than Pt and PtM (M = Ni, Fe, Cu) on graphene nanoplatelets prepared by simultaneous and subsequential deposition [54,55]. Furthermore, the value is comparable to that of NiSe/CP [56], $Ni_{0.85}Se$/CP [56], and Fe-Ni@C [57], for instance, though higher than that of NiSe-$Ni_{0.85}Se$/CP [56], Fe-Ni@NC-CNTs [57], and Fe-Ni@NC-powder [57]. Still, it should be kept in mind that the reported values are determined under different conditions.

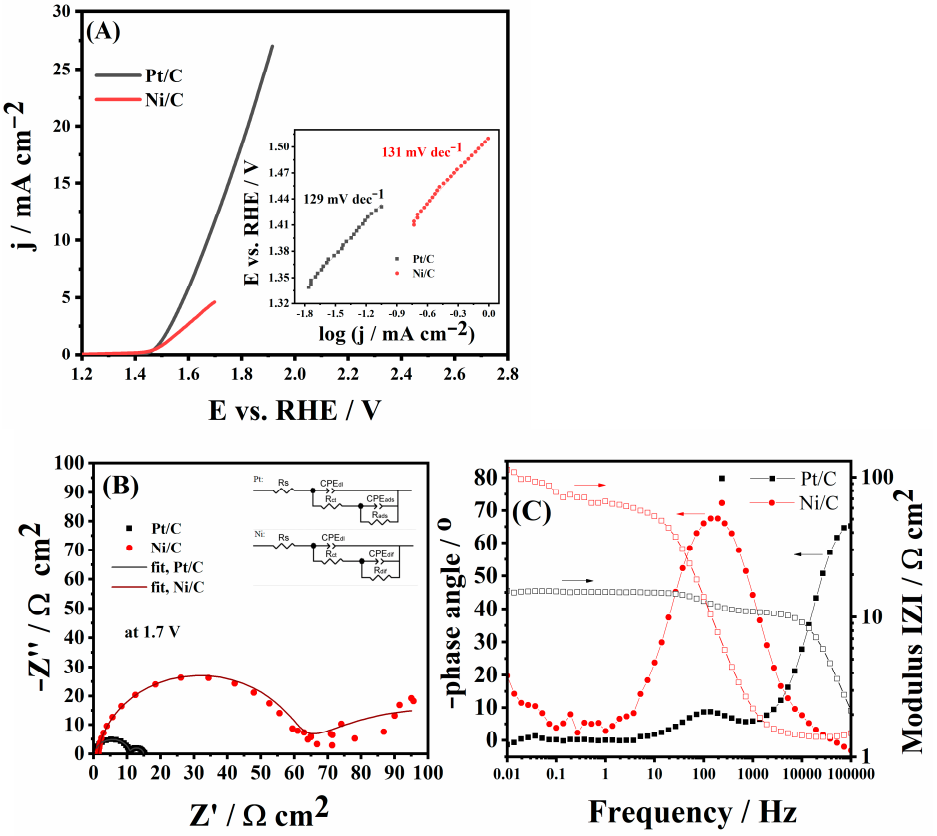


Figure 4. (**A**) Polarization curves of Pt/C and Ni/C at 5 mV s^{-1}, with the corresponding Tafel plots in the inset. (**B**) Nyquist and (**C**) Bode plots corresponding to the OER on Pt/C and Ni/C at 1.7 V (the arrows indicate the corresponding Y-axis). All measurements were conducted in 8 M KOH at 25 °C.

Table 3. Comparison of the performance of different electrocatalysts based on Pt and Ni for OER in alkaline medium.

Electrocatalyst	Electrolyte	b/mV dec^{-1}	Source
Pt/C	8 M KOH	129	This work
Ni/C	8 M KOH	131	This work
NiSe-$Ni_{0.85}Se$/CP	1 M KOH	98	[56]
Pt/GNPs	0.1 M KOH	478	[55]
PtNi/GNPs (simultaneously)	0.1 M KOH	356	[55]
PtFe/GNPs (simultaneously)	0.1 M KOH	280	[55]
PtCu/GNPs (simultaneously)	0.1 M KOH	490	[55]
sqPtNi/GNPs (sequentially)	0.1 M KOH	355	[54]
sqPtFe/GNPs (sequentially)	0.1 M KOH	307	[54]
sqPtCo/GNPs (sequentially)	0.1 M KOH	454	[54]
NiSe/CP	1 M KOH	138	[56]
$Ni_{0.85}Se$/CP	1 M KOH	210	[56]
Fe-Ni@C	1 M KOH	179	[57]
Fe-Ni@NC-CNTs	1 M KOH	45.5	[57]
Fe-Ni@NC-powder	1 M KOH	56.4	[57]
Ir/C	1 M KOH	43.7	[57]

GNP—graphene nanoplatelets; CP—carbon paper; NC—N-doped carbon; CNTs—carbon nanotubes.

More information about the electrocatalytic activity of Pt/C and Ni/C electrodes for OER was obtained through EIS. The spectra of both electrocatalysts are characterized by two-time constants, Figure 4B,C. For the Pt/C, two-phase angle maxima are observed in the high and intermediate frequency regions of the Bode plot, manifested as two clearly defined arcs in the Nyquist plot, and can be attributed to the capacitive behavior of the double layer at the electrode/solution interface and adsorption of OER reaction intermediates, respectively [58,59]. For the Ni/C, beside the main phase angle peak at intermediate frequencies of the Bode plot, i.e., the arc in the Nyquist plot, related to the capacitive double layer behavior, a tail can be observed in the low-frequency region resembling the Warburg impedance, Figure 4B. This tail can be ascribed to the impedance contribution resulting from the diffusion of the electroactive species in the solution.

The spectra fitting and analyses were performed using the equivalent circuits presented in Figure 4B, inset. The designation of the impedance elements is equivalent to that presented for the HER, except that the elements related to the diffusion of the species in the solution are denoted by "dif" in the index.

A glance at the double layer parameters reveals n_{dl} values slightly lower than 1 for both metal/carbon electrocatalysts, Table 4, indicating double layer behavior close to that of an ideal capacitor. On the other hand, the $n_{ads/dif}$ value of ~0.5, estimated for the Ni/C, is typical of Warburg impedance. For the OER, both metal/carbon electrocatalysts exhibit C_{dl} values significantly lower than those observed for HER, Tables 2 and 4, suggesting a lower number of OER active sites. However, the C_{dl} value of the Ni/C is still larger than the corresponding one of the Pt/C, around 45 times.

Table 4. EIS parameters of OER on Pt/C and Ni/C electrocatalysts at 1.7 V, obtained by EIS spectra fitting.

	R_s (Ω cm^2)	R_{ct} (Ω cm^2)	Q_{dl} (S cm^{-2} s^n)	n_{dl}	C_{dl} (F cm^{-2})	$R_{ads/dif}$ (Ω cm^2)	$Q_{ads/dif}$ (S cm^{-2} s^n)	$n_{ads/dif}$
Pt/C	0.36 ± 0.02	10.5 ± 0.1	$(1.43 \pm 0.04)\cdot10^{-6}$	0.96 ± 0.01	$(8.5 \pm 0.2)\cdot10^{-7}$	4.08 ± 0.04	$(5.8 \pm 0.4)\cdot10^{-4}$	0.94 ± 0.01
Ni/C	1.40 ± 0.02	59 ± 2	$(5.8 \pm 0.3)\cdot10^{-5}$	0.93 ± 0.01	$(3.9 \pm 0.2)\cdot10^{-5}$	80 ± 10	0.041 ± 0.004	0.45 ± 0.06

Regarding the OER-related resistance values of the Pt/C, higher R_{ct} than R_{ads} demonstrates that the OER kinetics in the case of Pt/C is controlled by the charge transfer process, Table 4. On the other hand, considering the R_{ct} and R_{dif} values of the Ni/C, the contribution of the diffusion of the electroactive species to the OER kinetics is significant. Additionally, the R_{ct} of the Ni/C is considerably larger than that of the Pt/C, contrary to HER, Tables 2 and 4. This can be explained by the partial deterioration of the sp^2 ordering and an increase in the sp^3-hybridized carbon fraction in the potential region of OER, resulting in a decline in the electrical conductivity of the carbon-based material [51,60,61]. The larger sp^3 fraction also means weaker interactions between adsorbed hydroxyl radicals formed at the initial step of OER and the surface of the carbon-based electrocatalyst [61], which can affect the OER performance. This phenomenon is pronounced for the Ni/C, considering its higher carbon and lower metal fraction than those of the Pt/C, resulting in slower charge transfer in the case of Ni/C.

Considering the discussion above, higher OER-related resistance values are the crucial factor making the Ni/C a worse electrocatalyst for OER than the Pt/C, unlike the case of HER, despite larger double-layer capacitance observed for the Ni/C. Such behavior reflects the fact that not all ion-adsorption and desorption sites are necessarily electrocatalytic active sites; they also can be affected by non-Faradaic processes, and thus, the C_{dl} is not always a credible measure of Faradaic activity trends [62]. This emphasizes the importance of thoroughly considering all impedance contributions to properly estimate the true electrocatalytic performance of the studied materials. Finally, the presented EIS results regarding

the OER performance of the metal/carbon electrocatalysts are in accordance with those deduced from the LSV polarization measurements, Figure 4A.

3.5. Catalysts' Stability for HER and OER

Furthermore, alongside the kinetic parameters obtained from linear voltammetry, the stability and durability of electrocatalysts represent another crucial factor in assessing their viability for potential applications under operational conditions. The stability of Pt/C and Ni/C was evaluated through chronoamperometry at a constant potential for 4500 s, as illustrated in Figure 5. Notably, materials demonstrate sustained activity over time, manifesting stability under both hydrogen and OER conditions. Fluctuations in current densities observed for Pt/C, particularly evident under conditions conducive to the OER, are believed to originate from pronounced O_2 gas evolution and robust bubbling rather than the instability of the material itself.

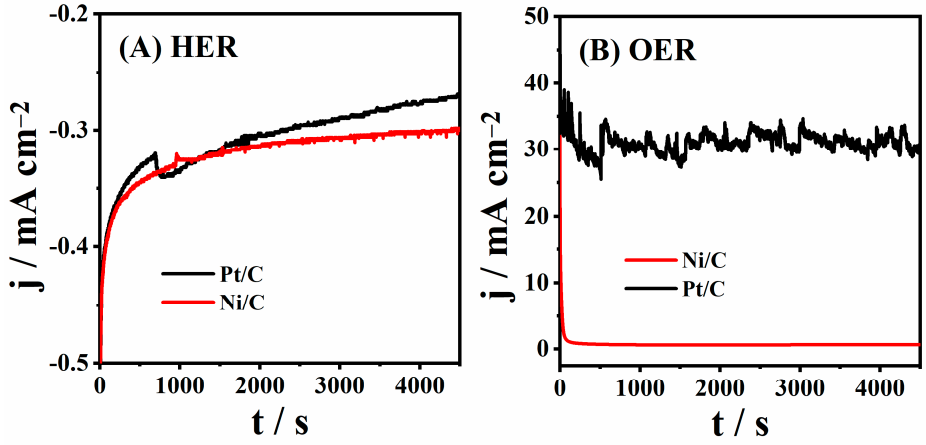


Figure 5. Chronoamperometric curves of Pt/C and Ni/C in 8 M KOH under conditions of (**A**) hydrogen evolution and (**B**) oxygen evolution at 25 °C.

4. Conclusions

This study underscores the pivotal role of metal-containing ionic liquids in tailoring the properties of carbon-based materials for electrocatalytic applications. The synergistic interactions between the metal nanoparticles and the carbon matrix enhanced catalytic performance. Specifically, the presence of Pt in the carbon matrix was found to augment the catalytic activity for oxygen evolution with a current density of 10 mA cm^{-2} recorded at a potential of 1.67 V and a Tafel slope of 129 mV dec^{-1}. Conversely, incorporating Ni leads to enhanced catalytic performance towards hydrogen evolution. Furthermore, materials demonstrated stable activity over time. The synthesis suggested here holds promise for the rational design and engineering of highly efficient electrocatalysts for energy conversion and storage applications. Future studies will be directed towards a more systematic investigation of the ionic liquids' cation and anion influence on the final materials' properties and electrocatalytic performance. Ionic liquids containing nickel will be chosen for these studies, aiming toward a more cost-effective and sustainable solution.

Supplementary Materials: The following supporting information can be downloaded at: https://www.mdpi.com/article/10.3390/pr13030623/s1, Figure S1: Scanning electron microscopy images of Ni/C at two different magnifications (analysis done using Phenom™ ProX Desktop scanning electron microscope, ThermoFisher Scientific ™, Waltham, MA, USA); Figure S2: TGA/DTA curves of Ni/C and Pt/C.

Author Contributions: Conceptualization, N.Z., D.M.F.S. and B.Š.; formal analysis, J.G., J.M. and D.J.; investigation, J.G., N.Z., M.V. (Milan Vraneš), J.M., M.V. (Milica Vasić) and D.J.; writing—original draft preparation, J.G., N.Z., M.V. (Milica Vasić) and D.J.; writing—review and editing, D.M.F.S. and B.Š.; visualization, J.G., M.V. (Milica Vasić) and J.M.; supervision, B.Š. All authors have read and agreed to the published version of the manuscript.

Funding: This research was funded by Fundação para a Ciência e Tecnologia (contract 2023.09426. CEECIND, D.M.F. Santos) and by the Ministry of Science, Technological Development and Innovation of the Republic of Serbia, grant number 451-03-136/2025-03/200017, 451-03-136/2025-03/200146, and 451-03-137/2025-03/200146.

Data Availability Statement: The data presented in this study are available on request from the corresponding author. The data are not publicly available due to privacy restrictions.

Conflicts of Interest: The authors declare no conflict of interest.

References

1. Barbir, F. Transition to renewable energy systems with hydrogen as an energy carrier. *Energy* **2009**, *34*, 308–312. [CrossRef]
2. Mazloomi, K.; Gomes, C. Hydrogen as an energy carrier: Prospects and challenges. *Renew. Sustain. Energy Rev.* **2012**, *16*, 3024–3033. [CrossRef]
3. Kanoglu, M.; Ayanoglu, A.; Abusoglu, A. Exergoeconomic assessment of a geothermal assisted high temperature steam electrolysis system. *Energy* **2011**, *36*, 4422–4433. [CrossRef]
4. Holladay, J.D.; Hu, J.; King, D.L.; Wang, Y. An overview of hydrogen production technologies. *Catal. Today* **2009**, *139*, 244–260. [CrossRef]
5. Mazloomi, S.K.; Sulaiman, N. Influencing factors of water electrolysis electrical efficiency. *Renew. Sustain. Energy Rev.* **2012**, *16*, 4257–4263. [CrossRef]
6. Zhang, C.; Bai, T.; Sun, Y.; Xin, B.; Zhang, S. Ionic Liquid/Deep Eutectic Solvent-Mediated Ni-Based Catalysts and Their Application in Water Splitting Electrocatalysis. *Catalysts* **2022**, *12*, 928. [CrossRef]
7. Šljukić, B.; Vujković, M.; Amaral, L.; Santos, D.M.F.; Rocha, R.P.; Sequeira, C.A.C.; Figueiredo, J.L. Carbon-supported Mo_2C electrocatalysts for hydrogen evolution reaction. *J. Mater. Chem. A* **2015**, *3*, 15505–15512. [CrossRef]
8. Šljukić, B.; Santos, D.M.F.; Vujković, M.; Amaral, L.; Rocha, R.P.; Sequeira, C.A.C.; Figueiredo, J.L. Molybdenum Carbide Nanoparticles on Carbon Nanotubes and Carbon Xerogel: Low-Cost Cathodes for Hydrogen Production by Alkaline Water. *Electrolysis Chemsuschem* **2016**, *9*, 1200–1208. [CrossRef]
9. Abu Hatab, A.S.; Ahmad, Y.H.; Abdul Rahman, M.B.; Al-Qaradawi, S.Y. Solution combustion synthesis of Ni-based hybrid metal oxides for oxygen evolution reaction in alkaline medium. *RSC Adv.* **2022**, *12*, 1694–1703. [CrossRef] [PubMed]
10. Zhang, Z.; Lei, Y.; Huang, W. Recent progress in carbon-based materials boosting electrochemical water splitting. *Chin. Chem. Lett.* **2022**, *33*, 3623–3631. [CrossRef]
11. Khalate, S.A.; Kadam, S.A.; Ma, Y.R.; Kulkarni, S.B.; Parale, V.G.; Patil, U.M. Binder free cobalt iron phosphate thin films as efficient electrocatalysts for overall water splitting. *J. Colloid Interface Sci.* **2022**, *613*, 720–732. [CrossRef]
12. Hao, L.; Wang, L.H.; Zhang, Y.H.; Qi, Y.F.; Tang, H.H.; Huang, Z.Q.; Yue, K.F.; Li, D.S.; Wang, Y.Y. Fe-doped CoFe–P phosphides nanosheets dispersed on nickel foam derived from Prussian blue analogues as efficient electrocatalysts for the oxygen evolution reaction. *J. Solid State Chem.* **2022**, *311*, 123084. [CrossRef]
13. Wang, X.; Wang, C.; Lai, F.; Sun, H.; Yu, N.; Geng, B. Self-Supported CoFe-P Nanosheets as a Bifunctional Catalyst for Overall Water Splitting. *ACS Appl. Nano Mater.* **2021**, *4*, 12083–12090. [CrossRef]
14. Milikić, J.; Knežević, S.; Ognjanović, M.; Stanković, D.; Rakočević, L.; Šljukić, B. Template-based synthesis of Co_3O_4 and Co_3O_4/SnO_2 bifunctional catalysts with enhanced electrocatalytic properties for reversible oxygen evolution and reduction reaction. *Int. J. Hydrogen Energy* **2023**, *48*, 27568–27581. [CrossRef]
15. Milikić, J.; Stojanović, S.; Damjanović-Vasilić, L.; Vasilić, R.; Šljukić, B. Efficient bifunctional cerium-zeolite electrocatalysts for oxygen evolution and oxygen reduction reactions in alkaline media. *Synth. Met.* **2023**, *292*, 117231. [CrossRef]
16. Xie, X.; Du, L.; Yan, L.; Park, S.; Qiu, Y.; Sokolowski, J.; Wang, W.; Shao, Y. Oxygen Evolution Reaction in Alkaline Environment: Material Challenges and Solutions. *Adv. Funct. Mater.* **2022**, *32*, 2110036. [CrossRef]
17. Xiong, Y.; He, P. A review on electrocatalysis for alkaline oxygen evolution reaction (OER) by Fe-based catalysts. *J. Mater. Sci.* **2023**, *58*, 2041–2067. [CrossRef]
18. Al-Naggar, A.H.; Shinde, N.M.; Kim, J.S.; Mane, R.S. Water splitting performance of metal and non-metal-doped transition metal oxide electrocatalysts. *Coord. Chem. Rev.* **2023**, *474*, 214864. [CrossRef]

19. Do, H.H.; Nguyen, T.H.C.; Truong, H.B.; Kim, S.Y.; Van Le, Q. Cobalt compounds-based hollow structure electrocatalysts for water splitting: A review. *Int. J. Hydrogen Energy* **2024**, *49*, 613–632. [CrossRef]
20. Kamaruzaman, N.A.; Zin, W.M.K.W.M.; Kamarudin, K.H.; Saleh, N.M.; Yusoff, F. Recent advances in transition metals-based materials as electrocatalysts for water splitting. *Int. J. Electrochem. Sci.* **2023**, *18*, 100187. [CrossRef]
21. Besleaga, I.; Fesenko, A.A.; Paul, A.; Šljukić, B.; Rapta, P.; Pombeiro, A.J.L.; Shutalev, A.D.; Arion, V.B. Nickel(ii) complexes with 14-membered bis-thiosemicarbazide and bis-isothiosemicarbazide ligands: Synthesis, characterization and catalysis of oxygen evolution reaction. *Dalt. Trans.* **2024**, *53*, 15826–15841. [CrossRef] [PubMed]
22. Bai, Y.; Yu, Z.; Tsekouras, G.; Cheng, Z. Recent advances in Ni-Fe Oxy hydroxide electrocatalysts for the oxygen evolution reaction in alkaline electrolyte targeting industrial applications. *Nano Sel.* **2021**, *3*, 766–791. [CrossRef]
23. Song, Y.; Xie, W.; Shao, M.; Duan, X. Integrated electrocatalysts derived from metal organic frameworks for gas-involved reactions. *Nano Mater. Sci.* **2023**, *5*, 161–176. [CrossRef]
24. Zdolšek, N.; Vujković, M.; Metin, Ö.; Brković, S.; Jocić, A.; Dimitrijević, A.; Trtić-Petrović, T.; Šljukić, B. Boosting electrocatalysis of oxygen reduction and evolution reactions with cost-effective cobalt and nitrogen-doped carbons prepared by simple carbonization of ionic liquids. *Int. J. Hydrogen Energy* **2022**, *47*, 14847–14858. [CrossRef]
25. Zdolšek, N.; Dimitrijević, A.; Bendova, M.; Krstić, J.; Rocha, R.P.; Figueiredo, J.L.; Bogdanovic, B.; Petrović, T.; Šljukić, B. Electrocatalytic Activity of Ionic-Liquid-Derived Porous Carbon Materials for the Oxygen Reduction Reaction. *ChemElectroChem* **2018**, *5*, 1037–1046. [CrossRef]
26. Milikic, J.; Oliviera, R.C.P.; Tapia, A.; Santos, D.M.F.; Zdolsek, N.; Trtic-Petrovic, T.; Vranes, M.; Sljukic, B. Ionic Liquid-Derived Carbon-Supported Metal Electrocatalysts. *Catalysts* **2021**, *11*, 632. [CrossRef]
27. Gidi, L.; Arce, R.; Ibarra, J.; Isaacs, M.; Aguirre, M.J.; Ramírez, G. Hydrogen evolution reaction highly electrocatalyzed by MWCNT/N-octylpyridinum hexafluorophosphate metal-free system. *Electrochim. Acta* **2021**, *372*, 137859. [CrossRef]
28. Shahsavarifar, S.; Masteri-Farahani, M.; Ganjali, M.R. Design and application of a polyoxometalate-ionic liquid-graphene oxide hybrid nanomaterial: New electrocatalyst for water oxidation, Colloids Surfaces A Physicochem. *Eng. Asp.* **2022**, *632*, 127812. [CrossRef]
29. Li, T.; Chen, Y.; Hu, W.; Yuan, W.; Zhao, Q.; Yao, Y.; Zhang, B.; Qiu, C.; Li, C.M. Ionic liquid in situ functionalized carbon nanotubes as metal-free catalyst for efficient electrocatalytic hydrogen evolution reaction. *Nanoscale* **2021**, *13*, 4444–4450. [CrossRef]
30. Liu, G.; Wang, B.; Ding, P.; Ye, Y.; Wei, W.; Zhu, W.; Xu, L.; Xia, J.; Li, H. Reactable ionic liquid in situ-induced synthesis of Fe_3O_4 nanoparticles modified N-doped hollow porous carbon microtubes for boosting multifunctional electrocatalytic activity. *J. Alloys Compd.* **2019**, *797*, 849–858. [CrossRef]
31. Wallace, A.G.; Symes, M.D. Water-Splitting Electrocatalysts Synthesized Using Ionic Liquids. *Trends Chem.* **2019**, *1*, 247–258. [CrossRef]
32. Chen, K.; Xu, B.; Shen, L.; Shen, D.; Li, M.; Guo, L.H. Functions and performance of ionic liquids in enhancing electrocatalytic hydrogen evolution reactions: A comprehensive review. *RSC Adv.* **2022**, *12*, 19452–19469. [CrossRef] [PubMed]
33. Miao, L.; Song, Z.; Zhu, D.; Li, L.; Gan, L.; Liu, M. Ionic Liquids for Supercapacitive Energy Storage: A Mini-Review. *Energy Fuels* **2021**, *35*, 8443–8455. [CrossRef]
34. Zhang, S.; Dokko, K.; Watanabe, M. Carbon materialization of ionic liquids: From solvents to materials. *Mater. Horiz.* **2015**, *2*, 168–197. [CrossRef]
35. Le Bail, J.A.; Duroy, H.; Fourquet, J.L. Ab-initio structure determination of $LiSbWO_6$ by X-ray powder diffraction. *Mat. Res. Bull.* **1988**, *23*, 447–452. [CrossRef]
36. Cheary, R.W.; Coelho, A. Fundamental parameters approach to x-ray line-profile fitting. *J. Appl. Crystallogr.* **1992**, *25*, 109–121. [CrossRef]
37. Magnin, Y.; Villermaux, E.; Amara, H.; Bichara, C.; Pellenq, R.J.M. Morphology control of metallic nanoparticles supported on carbon substrates in catalytic conditions. *Carbon* **2020**, *159*, 504–511. [CrossRef]
38. Zappielo, C.D.; Nanicuacua, D.M.; Santos, W.N.L.D.; Da Silva, D.L.F.; Dall'antônia, L.H.; De Oliveira, F.M.; Clausen, D.N.; Tarley, C.R.T. Solid Phase Extraction to On-Line Preconcentrate Trace Cadmium Using Chemically Modified Nano-Carbon Black with 3-Mercaptopropyltrimethoxysilane. *J. Braz. Chem. Soc.* **2016**, *27*, 1715–1726. [CrossRef]
39. Marjani, A.; Nakhjiri, A.T.; Adimi, M.; Jirandehi, H.F.; Shirazian, S. Modification of polyethersulfone membrane using MWCNT-NH2 nanoparticles and its application in the separation of azeotropic solutions by means of pervaporation. *PLoS ONE* **2020**, *15*, e0236529. [CrossRef] [PubMed]
40. Mojoudi, N.; Mirghaffari, N.; Soleimani, M.; Shariatmadari, H.; Belver, C.; Bedia, J. Phenol adsorption on high microporous activated carbons prepared from oily sludge: Equilibrium, kinetic and thermodynamic studies. *Sci. Rep.* **2019**, *9*, 19352. [CrossRef] [PubMed]
41. Liu, Z.; Huang, Y.; Zhao, G. Preparation and characterisation of activated carbon fibers from liquefied wood by ZnCl2 activation. *BioResources* **2016**, *11*, 3178–3190. [CrossRef]

42. Mahmoudian, M.; Khazani, Y.; Balkanloo, P.G.; Enayati, M. Poly(diallyldimethylammonium chloride)-grafted carboxylated-MWCNT as an additive in the polyethersulfone membrane. *Polym. Bull.* **2021**, *78*, 4313–4332. [CrossRef]
43. Metwally, N.H.; Saad, G.R.; El-Wahab, E.A.A. Grafting of multiwalled carbon nanotubes with pyrazole derivatives: Characterisation, antimicrobial activity and molecular docking study. *Int. J. Nanomed.* **2019**, *14*, 6645–6659. [CrossRef] [PubMed]
44. Moyo, M.; Nyamhere, G.; Sebata, E.; Guyo, U. Kinetic and equilibrium modelling of lead sorption from aqueous solution by activated carbon from goat dung. *Desalin. Water Treat.* **2016**, *57*, 765–775. [CrossRef]
45. Liu, Y.; Liu, X.; Dong, W.; Zhang, L.; Kong, Q.; Wang, W. Efficient Adsorption of Sulfamethazine onto Modified Activated Carbon: A Plausible Adsorption Mechanism. *Sci. Rep.* **2017**, *7*, 12437. [CrossRef] [PubMed]
46. Claramunt, S.; Varea, A.; López-Díaz, D.; Velázquez, M.M.; Cornet, A.; Cirera, A. The importance of interbands on the interpretation of the Raman spectrum of graphene oxide. *J. Phys. Chem. C* **2015**, *119*, 10123–10129. [CrossRef]
47. Adesuji, E.T.; Khalil-Cruz, L.E.; Videa, M.; Sánchez-Domínguez, M.; Costa, F.R.; Franco, D.V.; Da Silva, L.M.; Brug, G.J.; van den Eeden, A.L.G.; Sluyters-Rehbach, M.; et al. From nano to macro: Hierarchical platinum superstructures synthesized using bicontinuous microemulsion for hydrogen evolution reaction. *Electrochim. Acta* **2021**, *176*, 332–343. [CrossRef]
48. Growcock, F.B.; Jasinski, R.J. Time-Resolved Impedance Spectroscopy of Mild Steel in Concentrated Hydrochloric Acid. *J. Electrochem. Soc.* **1989**, *136*, 2310–2314. [CrossRef]
49. Brug, G.J.; van den Eeden, A.L.G.; Sluyters-Rehbach, M.; Sluyters, J.H. The analysis of electrode impedances complicated by the presence of a constant phase element. *J. Electroanal. Chem.* **1984**, *176*, 275–295. [CrossRef]
50. Qiu, Z.; Ma, Y.; Niklasson, G.A.; Edvinsson, T. An Electrochemical Impedance Study of Alkaline Water Splitting Using Fe Doped NiO Nanosheets. *Physchem* **2021**, *1*, 69–81. [CrossRef]
51. Dasgupta, D.; Demichelis, F.; Tagliaferro, A. Electrical conductivity of amorphous carbon and amorphous hydrogenated carbon. *Philos. Mag. B* **1991**, *63*, 1255–1266. [CrossRef]
52. Zhang, C.C.; Hartlaub, S.; Petrovic, I.; Yilmaz, B. Raman Spectroscopy Characterisation of Amorphous Coke Generated in Industrial Processes. *ACS Omega* **2022**, *7*, 2565–2570. [CrossRef] [PubMed]
53. Li, J.; Kim, S.J.; Han, S.; Chae, H. Characterisation of sp2/sp3 hybridisation ratios of hydrogenated amorphous carbon films deposited in C_2H_2 inductively coupled plasmas. *Surf. Coat. Technol.* **2021**, *422*, 127514. [CrossRef]
54. Mladenović, D.; Daş, E.; Santos, D.M.F.; Yurtcan, A.B.; Miljanić, Š.; Šljukić, B. Boosting oxygen electrode kinetics by addition of cost-effective transition metals (Ni, Fe, Cu) to platinum on graphene nanoplatelets. *J. Alloys Compd.* **2022**, *905*, 164156. [CrossRef]
55. Mladenović, D.; Daş, E.; Santos, D.M.F.; Yurtcan, A.B.; Šljukić, B. Highly Efficient Oxygen Electrode Obtained by Sequential Deposition of Transition Metal-Platinum Alloys on Graphene Nanoplatelets. *Materials* **2023**, *16*, 3388. [CrossRef] [PubMed]
56. Chen, Y.; Ren, Z.; Fu, H.; Zhang, X.; Tian, G. NiSe-Ni0.85Se heterostructure nanoflake arrays on carbon paper as efficient electrocatalysts for overall water splitting. *Small* **2018**, *14*, 1800763. [CrossRef] [PubMed]
57. Zhao, X.; Pachfule, P.; Li, S.; Simke, J.R.J.; Schmidt, J.; Thomas, A. Bifunctional electrocatalysts for overall water splitting from an iron/nickel-based bimetallic metal–organic framework/dicyandiamide composite. *Angew. Chem.* **2018**, *57*, 8921–8926. [CrossRef] [PubMed]
58. Costa, F.R.; Franco, D.V.; Da Silva, L.M. Electrochemical impedance spectroscopy study of the oxygen evolution reaction on a gas-evolving anode composed of lead dioxide microfibers. *Electrochim. Acta* **2013**, *90*, 332–343. [CrossRef]
59. Jeon, S.S.; Kang, P.W.; Klingenhof, M.; Lee, H.; Dionigi, F.; Strasser, P. Active Surface Area and Intrinsic Catalytic Oxygen Evolution Reactivity of NiFe LDH at Reactive Electrode Potentials Using Capacitances. *ACS Catal.* **2023**, *13*, 1186–1196. [CrossRef]
60. Santini, C.A.; Sebastian, A.; Marchiori, C.; Jonnalagadda, V.P.; Dellmann, L.; Koelmans, W.W.; Rossell, M.D.; Rossel, C.P.; Eleftheriou, E. Oxygenated amorphous carbon for resistive memory applications. *Nat. Commun.* **2015**, *6*, 8600. [CrossRef] [PubMed]
61. Honda, K.; Naragino, H.; Shimai, Y. Control of Electric Conductivity and Electrochemical Activity of Hydrogenated Amorphous Carbon by Incorporating Boron Atoms. *J. Electrochem. Soc.* **2014**, *161*, B207–B215. [CrossRef]
62. Anantharaj, S.; Sugime, H.; Noda, S. Why shouldn't double-layer capacitance (C_{dl}) be always trusted to justify Faradaic electrocatalytic activity differences? *J. Electroanal. Chem.* **2021**, *903*, 115842. [CrossRef]

Disclaimer/Publisher's Note: The statements, opinions and data contained in all publications are solely those of the individual author(s) and contributor(s) and not of MDPI and/or the editor(s). MDPI and/or the editor(s) disclaim responsibility for any injury to people or property resulting from any ideas, methods, instructions or products referred to in the content.